

Triply polarized WWW at the LHC: first glimpse at LO

Van Cuong Le, Duc Ninh Le, Thi Nhung Dao

Phenikaa Institute for Advanced Study, Phenikaa University, Hanoi 12116, Vietnam

E-mail: lvcuong.98tv@gmail.com, ninh.leduc@phenikaa-uni.edu.vn,
nhung.daothi@phenikaa-uni.edu.vn

ABSTRACT: We present first results for triply polarized WWW events at the LHC. The calculation is performed at leading order for fully leptonic decays using the Standard Model. Employing an inclusive kinematic cut setup, we found that the triply-transverse polarization fraction is about 51%, while the triply-longitudinal (LLL) fraction is smallest with 1.4% for the $W^-W^+W^+$ process. The interference between different polarization amplitudes amounts to +1.8%. Results for the $W^+W^-W^-$ case are similar. Based on known higher-order results for the diboson processes, radiative corrections are not expected to increase the LLL fraction to the level of tens of percent. This means that measuring the LLL cross section at the LHC will be very challenging. A new on-shell mapping for triboson processes, being a crucial element of polarized cross-section calculation, is also presented.

Contents

1	Introduction	1
2	Details of calculation	2
2.1	On-shell mapping for $V_1V_2V_3$ production	5
2.2	Code implementation	8
3	Numerical results	8
3.1	Input parameters	8
3.2	Integrated cross sections	9
3.3	Kinematic distributions	12
4	Conclusions	15
A	Results for the $W^+W^-W^-$ process	16

1 Introduction

Finding new physics beyond the Standard Model (SM) is not easy. Precision is really the key in this effort.

The Large Hadron Collider (LHC), where two bunches of protons are collided at 13.6 TeV, is a great playground to understand the boundaries of particle physics. The ATLAS and CMS detectors have been able to distinguish the top quarks, massive gauge bosons, and Higgs boson, produced in the collisions. Moreover, different polarized states of the massive gauge bosons have been observed in diboson processes [1–3]. These measurements of polarized cross sections are based on template-fitting methods, where polarization templates are produced by simulation. Polarization and quantum entanglement observables of top-quark pairs have also recently been measured [4, 5].

Knowing polarization templates with high precision is therefore important here. For inclusive diboson processes, results at the level of next-to-next-to-leading order (NNLO) QCD and next-to-leading order (NLO) electroweak (EW) have recently been achieved (see [6–8] for key information). Polarized vector boson scattering has been studied in [9] for WZ case and [10] for same-sign W^+W^+ case. It is possible to calculate individually polarized cross sections thanks to a technique named Double Pole Approximation (DPA) which guarantees gauge invariance.

Parton shower is important for the improvement of the fixed-order results as well as the generation of events. This has been done for polarized diboson in [11] at NLO QCD level, and for polarized multi-boson at approximate NLO QCD [12].

In this work, we take the first step for the calculation of polarized cross sections of the inclusive triboson processes. The triple W production is chosen as an illustration. A new ingredient is the on-shell mapping needed for the Triple Pole Approximation (TPA). A general and robust method, applicable for all triboson processes, is identified in this study. This helps us to obtain numerical results for triply-polarized cross sections of the WWW processes. First results at leading order (LO) are presented in this work.

Our presentation is outlined as follows. The definition of polarized cross sections using the TPA is given in Section 2. The new on-shell mapping is presented in Section 2.1 and details of our code implementation in Section 2.2. Numerical results for the $W^-W^+W^+$ process are provided in Section 3, while those of the $W^+W^-W^-$ case are in Appendix A. Conclusions are given in Section 4.

2 Details of calculation

We consider the following process:

$$p + p \rightarrow l_1 + l_2 + l_3 + l_4 + l_5 + l_6 + X, \quad (2.1)$$

where the final state can be $e^- \bar{\nu}_e \mu^+ \nu_\mu \tau^+ \nu_\tau$ or $e^+ \nu_e \mu^- \bar{\nu}_\mu \tau^- \bar{\nu}_\tau$. At LO, the contributing partonic processes are:

$$\bar{q}(k_1) + q'(k_2) \rightarrow l_1(k_3) + l_2(k_4) + l_3(k_5) + l_4(k_6) + l_5(k_7) + l_6(k_8), \quad (2.2)$$

with q and q' being the quarks of the first two generations. Representative Feynman diagrams at LO are shown in Fig. 1.

Among these 6-lepton events, we are interested in events coming from the polarized WWW system. These events are produced by the following processes:

$$\bar{q}(k_1) + q'(k_2) \rightarrow V_1(q_1) + V_2(q_2) + V_3(q_3) \rightarrow \sum_{i=1}^6 l_i(k_{i+2}), \quad (2.3)$$

where the intermediate $V_1 V_2 V_3$ can be $W^- W^+ W^+$ or $W^+ W^- W^-$, corresponding to the final state $e^- \bar{\nu}_e \mu^+ \nu_\mu \tau^+ \nu_\tau$ or $e^+ \nu_e \mu^- \bar{\nu}_\mu \tau^- \bar{\nu}_\tau$, respectively. These signal processes will therefore be referred to as $W^- W^+ W^+$ or $W^+ W^- W^-$ for short. Representative Feynman diagrams of this mechanism are displayed in Fig. 1 (a, b, c, d, k).

One observes that the diagrams belonging to this triply-resonant class, being a subset of the full process Eq. (2.2), do not form a gauge-invariant group for a general kinematic configuration. However, gauge-invariant results can be obtained by summing over on-shell kinematic configurations. These configurations can be calculated by means of an on-shell mapping as specified in Section 2.1. For these on-shell momentum configurations, denoted with a hat, we have:

$$\hat{q}_i = M_{V_i}^2, \quad i = 1, 2, 3. \quad (2.4)$$

With the intermediate gauge bosons satisfying these on-shell conditions, we can then factorize the helicity amplitude for the process Eq. (2.3) into gauge-invariant factors, being the

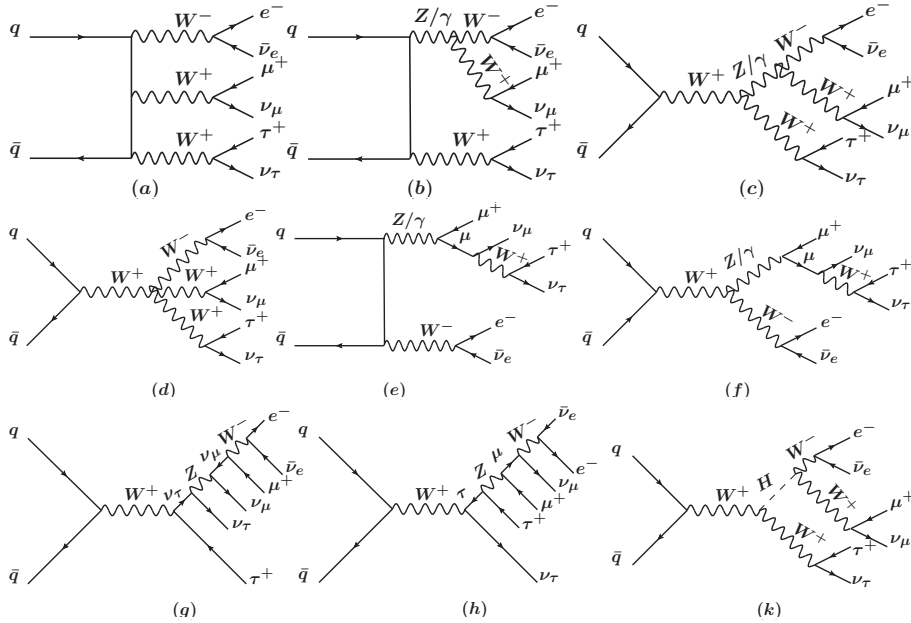


Figure 1: Representative Feynman diagrams at Born level for the full off-shell process, classified into the triply-resonant diagrams (a, b, c, d, k), doubly-resonant diagrams (e, f), singly-resonant diagrams (g, h), and WH diagram (k).

on-shell production amplitude $\bar{q}q' \rightarrow V_1 V_2 V_3$ and three on-shell decay amplitudes $V_i \rightarrow ll'$. Specifically, for a given helicity configuration of the initial-state quarks and final-state leptons, at leading order we have

$$\mathcal{A}_{\text{TPA}}^{\bar{q}q' \rightarrow V_1 V_2 V_3 \rightarrow 6l}([k_i]) = \frac{1}{Q_1 Q_2 Q_3} \sum_{\lambda_1, \lambda_2, \lambda_3=1}^3 \left[\mathcal{A}^{\bar{q}q' \rightarrow V_1 V_2 V_3}([k_i], \lambda_1, \lambda_2, \lambda_3) \mathcal{A}^{V_1 \rightarrow l_1 l_2}([k_i], \lambda_1) \mathcal{A}^{V_2 \rightarrow l_3 l_4}([\hat{k}_i], \lambda_2) \mathcal{A}^{V_3 \rightarrow l_5 l_6}([\hat{k}_i], \lambda_3) \right], \quad (2.5)$$

where

$$Q_i = q_i^2 - M_{V_i}^2 + iM_{V_i}\Gamma_{V_i} \quad (i = 1, 2, 3), \quad (2.6)$$

with the off-shell momenta $q_1 = k_3 + k_4$, $q_2 = k_5 + k_6$, $q_3 = k_7 + k_8$ and M_{V_i} , Γ_{V_i} being the pole mass and the total decay width of the resonance V_i , respectively. The index λ_i is the polarization (or helicity) index of the massive gauge boson V_i . $[k_i]$ is a set of off-shell external momenta, while $[\hat{k}_i]$ is a set of on-shell external momenta. In practice, $[\hat{k}_i]$ is obtained from $[k_i]$ by using an on-shell mapping, see Section 2.1. This mapping is not unique, but the results of different mappings are in good agreement within the intrinsic uncertainty of the approximation, being of the order of $\mathcal{O}(\Gamma_{V_i}/M_{V_i})$ [13]. The TPA is a straightforward extension of the DPA used for diboson production processes [13–15]. Recently, the DPA has been extensively used to define polarized cross sections of diboson processes at NLO EW and NNLO QCD levels [6, 7, 16]. The TPA has been employed in [17] for the case of unpolarized WWW production at the LHC.

From the TPA master equation Eq. (2.5) we then define the polarized cross sections as follows. For example, the LLL (triply longitudinal) cross section is calculated by selecting the term with $\lambda_1 = \lambda_2 = \lambda_3 = 2$ in the r.h.s. of Eq. (2.5). The TTT (triply transverse) one includes eight terms with $\lambda_i = 1$ or 3 (1 for left transverse, 3 for right transverse). Interference between these left-transverse and right-transverse modes are included in the TTT contribution. Other polarizations including TTL and TLL (the position of the L or T is unimportant) are similarly defined as:

$$\mathcal{A}_{\text{TTL}} = \sum_{\lambda_1, \lambda_2, \lambda_3 \in [1, 2, 3] \exists! \lambda_i = 2} \mathcal{A}_{\text{TPA}}(\lambda_1, \lambda_2, \lambda_3), \quad (2.7)$$

$$\mathcal{A}_{\text{TLL}} = \sum_{\lambda_1, \lambda_2, \lambda_3 \in [1, 2, 3] \exists! \lambda_i \in [1, 3]} \mathcal{A}_{\text{TPA}}(\lambda_1, \lambda_2, \lambda_3). \quad (2.8)$$

Taking the square of the modulus of these polarized amplitudes includes interference between various individual polarization modes, such as between $W_T^- W_T^+ W_L^+$ and $W_L^- W_T^+ W_T^+$ etc. While the unpolarized cross section is Lorentz invariant, polarized ones are not as the summation over the polarization indices is not complete. We therefore choose the VVV center-of-mass frame (c.m.f.) to define polarizations in this study. Practically, this means that the on-shell momenta must be calculated in the VVV c.m.f.. The off-shell denominators Q_i in Eq. (2.5) are Lorentz invariant, hence can be calculated in any reference frame.

The TPA unpolarized cross section reads

$$\sigma_{\text{TPA}}^{\text{unpol}} = \sigma_{\text{TTT}} + \sigma_{\text{TTL}} + \sigma_{\text{TLL}} + \sigma_{\text{LLL}} + \sigma_{\text{Inf}}, \quad (2.9)$$

where the last term is the polarization interference.

Solution for $[\hat{k}_i]$ exists when a certain kinematic condition is met. In particular, this requires

$$M_{6l} = \sqrt{\left(\sum_{i=3}^8 k_i\right)^2} > M_{V_1} + M_{V_2} + M_{V_3}. \quad (2.10)$$

This condition is necessary but not sufficient. The complete set of conditions, named TPA cuts, will be given in Section 2.1. The TPA cuts generally involve the individual momenta of the final-state neutrinos and charged leptons, with the only exceptional case being the ZZZ process with six charged leptons. Since the neutrino momenta are unknown in experimental analyses, the TPA cuts cannot be imposed in measurements. They must however be applied in the simulation of the polarized events.

Some important technical notes are in order. For the implementation of Eq. (2.5), it is crucial to note that the production and decay amplitudes depend on the on-shell momenta $[\hat{k}_i]$. Moreover, as the production and decay amplitudes are calculated using the stable V_i assumption (i.e. infinity-time limits for external states), the resonance decay widths Γ_{V_i} are neglected in these amplitudes. This means that Γ_{V_i} only occur in the prefactor $1/(Q_1 Q_2 Q_3)$ in Eq. (2.5). The other decay widths of unstable particles such as the Higgs boson, the

top quark or the other massive gauge boson not in the triple-resonance system (i.e. the Z boson in the present case) are kept in the calculation of those on-shell amplitudes. On the other hand, for the full off-shell calculation of the processes in Eq. (2.2), the decay widths of all unstable particles, including those in the $V_1V_2V_3$ system, are fully taken into account using the complex-mass scheme [18–20]. Further details of the input parameter scheme for the TPA and off-shell calculations are provided in Section 3.

2.1 On-shell mapping for $V_1V_2V_3$ production

In this section, we present a general on-shell mapping applicable for any triboson production process. The method has the following features: dynamic and democratic. It is dynamic in the sense that the mapping depends on the phase-space point. This is crucial to obtain a maximal size for the set of on-shell momentum configurations. It is democratic because it treats all the vector bosons equally. This is important to preserve the symmetry of the process. For example, for the case of the $W^-W^+W^+$ process at hand, a good on-shell mapping should treat the two W^+ equally, so that the $W_X^-W_L^+W_T^+$ and $W_X^-W_T^+W_L^+$ (with X being any polarization) polarized cross sections are the same.

The on-shell momentum configurations satisfy the following conditions:

$$\begin{aligned} \hat{k}_i^2 &= 0, \quad (k = 1, \dots, 8), \\ \hat{q}_1^2 &= (\hat{k}_3 + \hat{k}_4)^2 = M_{V_1}^2, \quad \hat{q}_2^2 = (\hat{k}_5 + \hat{k}_6)^2 = M_{V_2}^2, \quad \hat{q}_3^2 = (\hat{k}_7 + \hat{k}_8)^2 = M_{V_3}^2. \end{aligned} \quad (2.11)$$

For the initial state particles, we simply choose $\hat{k}_i = k_i$ with $i = 1, 2$. This leads to the following constraint on \hat{q}_i :

$$\hat{q}_1 + \hat{q}_2 + \hat{q}_3 = q_1 + q_2 + q_3 = q_{VVV}. \quad (2.12)$$

The next step is to obtain \hat{q}_i . The idea is to split the VVV system into two parts: A and B with A being a single particle while B containing two particles. This splitting is obviously not unique. We do not use a fixed splitting, say $A = V_1$ and $B = V_2V_3$, for all phase-space points. Rather, the splitting is dynamical and determined point-wise using certain criteria to be specified.

Assuming that this splitting has been done and we obtain two systems with momenta q_A and q_B in the VVV c.m.f.. We then perform a pseudo on-shell mapping for A and B , called OSMAP-AB, with the conditions

$$\hat{q}_A^2 = M_{V_i}^2, \quad \bar{q}_B^2 = m_B^2, \quad (2.13)$$

as done in [13] for W^+W^- and in [21] for WZ . Note that M_{V_i} is the pole mass of one of the identified V_i and $m_B^2 = (q_{V_j} + q_{V_k})^2$ is the off-shell invariant mass of the B system. The invariant mass of the B system does not change under this mapping. The bar notation for the B system is to indicate that this is not yet an on-shell momentum.

The key idea of this mapping is to fix the spatial direction of \hat{q}_A in the on-shell AB c.m.f. to be the same as that of q_A in the off-shell AB c.m.f.. Fixing the angles first is important to make sure that the projected momenta will lie in the physical region. Indeed,

the main point of the on-shell mapping is this choice of fixing the spatial direction in the center-of-mass frame, which we will repeatedly employ in the following steps.

The energy component of \hat{q}_A in the on-shell AB c.m.f. is easily calculated using the Eq. (2.13). We have:

$$\hat{E}_A = \frac{M_{V_i}^2 - m_B^2}{2m_{VVV}} + \frac{1}{2}M_{V_i}, \quad m_{VVV} = \sqrt{q_{VVV}^2}. \quad (2.14)$$

After this step, one then obtain \hat{q}_A and \bar{q}_B in the VVV frame with

$$\bar{q}_B = q_{VVV} - \hat{q}_A. \quad (2.15)$$

This solution exists when $|\vec{q}_A| = (\hat{E}_A^2 - M_{V_i}^2)^{1/2}$ is positively real, leading to:

$$m_{VVV} > M_{V_i} + m_B. \quad (2.16)$$

The next step is to decay B into two on-shell particles V_j and V_k . We again employ the OSMAP-AB as follows. We first imagine to be in the \bar{B} -rest frame and choose the spatial direction of \hat{q}_{V_j} to be the same as that of q_{V_j} in the $V_j V_k$ c.m.f.. Specifically, the spatial direction of q_{V_j} in the $V_j V_k$ frame (which is different from the \bar{B} -rest frame) is first calculated as:

$$\vec{n}_{V_j} = \frac{\vec{q}_{V_j}}{|\vec{q}_{V_j}|}. \quad (2.17)$$

Then, in the \bar{B} -rest frame we choose the unit vector as:

$$\vec{\hat{n}}_{V_j} = \vec{n}_{V_j}. \quad (2.18)$$

The energy component of \hat{q}_{V_j} in the \bar{B} -rest frame is simply calculated using the on-shell conditions:

$$\hat{q}_{V_j}^2 = M_{V_j}^2, \quad \hat{q}_{V_k}^2 = M_{V_k}^2. \quad (2.19)$$

We obtain:

$$\hat{E}_{V_j} = \frac{M_{V_j}^2 - M_{V_k}^2}{2m_B} + \frac{1}{2}M_{V_j}, \quad \hat{E}_{V_k} = m_B - \hat{E}_{V_j}. \quad (2.20)$$

The magnitude of the spatial momentum reads:

$$|\vec{q}_{V_j}| = \sqrt{\hat{E}_{V_j}^2 - M_{V_j}^2}. \quad (2.21)$$

This solution is real and positive when

$$m_B > M_{V_j} + M_{V_k}. \quad (2.22)$$

Eq. (2.16) and Eq. (2.22) are the necessary and sufficient conditions to have a solution for the on-shell momenta. These are the TPA cuts above mentioned. The condition Eq. (2.10)

is just a consequence of these cuts. In practice, the cut Eq. (2.10) can be implemented as soon as the off-shell momenta are known to improve the computation speed.

From Eq. (2.18) and Eq. (2.21) the on-shell momenta \hat{q}_{V_j} and \hat{q}_{V_k} are known in the \bar{B} -rest frame. We then boost them back to the VVV frame using the boost vector \bar{q}_B to complete the set of $\hat{q}_{V_i}, \hat{q}_{V_j}, \hat{q}_{V_k}$.

Now is the right position to discuss the splitting into A and B . The aim is to have a maximal size of the on-shell momentum configurations. This means that for each phase-space point under consideration we have to find an AB splitting satisfying the TPA cuts of Eq. (2.16) and Eq. (2.22). In total, there are three possibilities for choosing A . If there are more than one possibilities passing the TPA cuts, the one with smaller value of m_B is chosen. One can also choose the one with larger m_B . We have actually done this and found that both choices give very similar results (for integrated and differential cross sections). For integrated cross sections, the differences are within 0.2% for the TTT, TTL, and TLL. For the LLL, the choice of $\min(m_B)$ gives a slightly larger cross section, with a difference of 1.3%. Since the LLL polarization has a higher priority in polarization studies, the $\min(m_B)$ criterion is adopted in this work.

The final step is to perform the decays of $\hat{q}_{V_i}, \hat{q}_{V_j}, \hat{q}_{V_k}$ into leptons. One has to pay attention to the lepton assignment here. The simplest way is to re-order the momenta $\hat{q}_{V_i}, \hat{q}_{V_j}, \hat{q}_{V_k}$ such that \hat{q}_{V_1} is placed first, \hat{q}_{V_2} second, and \hat{q}_{V_3} last. One then do the following decays:

$$\hat{q}_{V_1} = \hat{k}_3 + \hat{k}_4, \quad \hat{q}_{V_2} = \hat{k}_5 + \hat{k}_6, \quad \hat{q}_{V_3} = \hat{k}_7 + \hat{k}_8, \quad (2.23)$$

using the same idea as above. For example, to find \hat{k}_3 and \hat{k}_4 , one imagines to be in the on-shell c.m.f. of 3 and 4 and choose the spatial direction of \hat{k}_3 to be that of k_3 calculated in the off-shell (3,4) c.m.f.. This is why we have to make the lepton assignment correctly. The energy component is calculated as usual using the on-shell conditions. Finally, one has to boost the on-shell momenta \hat{k}_3 and \hat{k}_4 to the VVV frame using the boost vector \hat{q}_{V_1} . This idea was used for the decay of $Z \rightarrow \ell\ell'$ in [6]. A very similar idea was used in [22], but with an important difference related to the choice of the spatial direction. In [22] the spatial direction of \hat{k}_3 is set equal to that of k_3 calculated in the *on-shell* (3,4) c.m.f.. Notice that the spatial momenta \vec{k}_3 and \vec{k}_4 are not back to back in the c.m.f. of \hat{q}_{V_1} .

We call the above method OSMAP-12 (12 indicates that one vector boson is on-shell projected in the first step, two bosons in the second step). In [22], a different procedure was suggested. The idea was to choose a pair, say $V_i V_j$, first. One then performs the on-shell mapping OSMAP-AB for these two resonances to obtain \hat{q}_{V_i} and \hat{q}_{V_j} . One of these on-shell momenta is then paired with the remaining resonance V_k and the same procedure is repeated to obtain the on-shell momenta \hat{q}_k . Compared to our procedure, the TPA condition in the second step is more hidden as it involves the on-shell projected momenta from the first step.

For comparison, we have implemented this procedure with the following improvements. In the first step, the pair $V_i V_j$ is dynamically chosen by checking the TPA condition of $(q_{V_i} + q_{V_j})^2 > (M_{V_i} + M_{V_j})^2$ and choosing the pair with smaller value of the invariant mass in case of multiple choices. In the second step, the on-shell momentum chosen to pair with

the q_{V_k} is the one with smaller value of the invariant mass if both choices pass the TPA condition. This method is named OSMAP-21.

We have checked that the numerical results (integrated and differential polarized cross sections) of the two methods OSMAP-12 and OSMAP-21 are very close. For the integrated cross sections, differences are within 0.1%, hence practically identical. The OSMAP-12 is chosen in this work because it gives a simple and clear picture of the TPA conditions.

Finally, Ref. [17] introduced another on-shell mapping for triboson production. We have however not yet performed any comparison with this as we do not see any advantage of this mapping.

2.2 Code implementation

The calculation of this work has been implemented in our private computer program MulBos (for MultiBoson production). This program was first created for calculating polarized cross sections of diboson processes. Results at the NLO QCD+EW level for WZ , W^+W^- , and ZZ have been published in [7, 23, 24]. This work marks the first extension of MulBos to the class of triboson processes.

The helicity amplitudes for the production and decay processes are generated by FeynArts [25] and FormCalc [26]. Phase-space integration is done using the Vegas Monte-Carlo method [27] as implemented in the computer program BASES [28]. Additional importance sampling is implemented in the phase-space generation step to smooth out the Breit-Wigner distributions of the resonances. This is done with the help of resonance mapping routines publicly available in the open-source code VBFNLO-3.0 [29].

For cross-checking purpose, we have performed two independent implementations. In one implementation, FeynArts-3.4 and FormCalc-6.0 were used to generate the helicity amplitudes. In the other, FeynArts-3.11 and FormCalc-9.10 were employed. Phase-space generation and on-shell mapping have been independently implemented. Results of the two codes agree within the statistical errors. Furthermore, for the full off-shell cross sections, good agreement with VBFNLO-3.0 has been found.

3 Numerical results

3.1 Input parameters

For the numerical results presented in this section, the proton-proton center-of-mass energy is $\sqrt{s} = 13.6$ TeV. As default, the factorization scale is chosen dynamically as $\mu = M_{6l}/2$. For the parton distribution functions (PDF), the set NNPDF40_lo_as_01180 [30] is used via the LHAPDF6 library [31].

Model parameters are $G_F = 1.1663788 \times 10^{-5}$ GeV⁻² (Fermi constant) and $M_W = 80.3692$ GeV, $M_Z = 91.1880$ GeV according to the latest data from Particle Data Group [32]. Other relevant parameters include $\Gamma_W = 2.14$ GeV, $\Gamma_Z = 2.4955$ GeV, $M_H = 125.20$ GeV, $\Gamma_H = 0.0037$ GeV. The leptons and quarks are approximated as massless. The top quark does not occur in this calculation.

For the TPA calculations, the electromagnetic coupling constant is obtained via the Fermi constant using $\alpha = \sqrt{2}G_F M_W^2(1 - M_W^2/M_Z^2)/\pi$. This gives $1/\alpha \approx 132.10015$ and $\sin^2 \theta_W = 1 - M_W^2/M_Z^2 \approx 0.22321$ with θ_W being the weak-mixing angle. For the full off-shell calculation (named full for short), the complex-mass scheme is used. At LO, this is simply done as follows. In the first step, the pole mass and total decay width of the W and Z bosons are shifted as (with $V = W, Z$):

$$\hat{M}_V = \frac{M_V}{\sqrt{1 + (\Gamma_V/M_V)^2}}, \quad \hat{\Gamma}_V = \frac{\Gamma_V}{\sqrt{1 + (\Gamma_V/M_V)^2}}. \quad (3.1)$$

Then, the idea is to replace M_V^2 with the complex mass $\tilde{M}_V^2 = \hat{M}_V^2 - i\hat{M}_V\hat{\Gamma}_V$ everywhere in the helicity amplitudes keeping the electromagnetic coupling constant $e = \sqrt{4\pi\alpha}$ as an independent real parameter. In particular the $\sin \theta_W$ and $\cos \theta_W$ are made complex with $\cos^2 \theta_W = \tilde{M}_W^2/\tilde{M}_Z^2$. The value of α is calculated as $\alpha = \sqrt{2}G_F\tilde{M}_W^2(1 - \tilde{M}_W^2/\tilde{M}_Z^2)/\pi$. Numerically, the new values of α and $\sin^2 \theta_W$ in the complex-mass scheme then read $1/\alpha \approx 132.21216$ and $\sin^2 \theta_W \approx 0.22319 - 5.73970 \times 10^{-4}i$, which are slightly shifted compared to the ones of the TPA.

Since our purpose is to survey the magnitudes of polarized cross sections across the whole phase space, focusing on the triple resonance region, a simple set of kinematic cuts has been used. They are:

$$P_{T,\ell} > 15 \text{ GeV}, \quad |\eta_\ell| \leq 2.7, \quad \Delta R(\ell, \ell') > 0.1, \\ m_{W^+W^-} > 130 \text{ GeV}, \quad (3.2)$$

where ℓ is a charged lepton (i.e. e, μ or τ), and $\Delta R(\ell, \ell') = \sqrt{(\eta_\ell - \eta_{\ell'})^2 + (\phi_\ell - \phi_{\ell'})^2}$ with ϕ_ℓ and η_ℓ being the azimuthal angle and pseudo-rapidity of the lepton ℓ . These cuts are implemented in the proton-proton c.m.f. (Lab frame). The W^+W^- invariant mass cut is to remove the $H \rightarrow 4$ leptons resonance which is of no interest in this study as we are focusing on the triple-resonance region. This cut has an impact in the full off-shell case. For the TPA calculations its effects are negligible due to the TPA cuts.

Before presenting our findings, we stress again here that the polarized cross sections are calculated in the WWW c.m.f..

3.2 Integrated cross sections

We first present results for the integrated cross sections. As the dependence on the factorization scale is an important issue for the estimation of theoretical uncertainties, we make a comparison here between two choices: fixed scale choice of $\mu_{\text{fix}} = \xi(3M_W)/2$ and the default dynamical scale $\mu_{\text{dyn}} = \xi M_{6l}/2$. Results for the case of $\xi = 1$ are provided in Table 1, while the ξ dependence is plotted in Fig. 2.

Besides the statistical uncertainties, the scale uncertainties are also provided in Table 1. They are calculated by deviating the scale from its central position (μ_0) by a factor of two, up and down. This gives asymmetric errors. The usual polarization fractions, calculated with respect to the unpolarized TPA result, are also given. The relative difference between the fixed-scale cross section and dynamical-scale one is calculated as $\delta_\sigma = (\sigma_{\text{fix}} - \sigma_{\text{dyn}})/\sigma_{\text{dyn}}$.

	σ_{fix} [ab]	f_{fix} [%]	σ_{dyn} [ab]	f_{dyn} [%]	δ_σ [%]
Full off-shell	122.29(2) ^{+0.06%} _{-0.46%}	–	120.13(2) ^{+0.00%} _{-0.28%}	–	+1.8
Unpol. TPA	118.38(2) ^{+0.15%} _{-0.60%}	100	116.52(2) ^{+0.00%} _{-0.37%}	100	+1.6
TTT	60.75(1) ^{+0.00%} _{-0.48%}	51.3	59.30(1) ^{+0.05%} _{-0.65%}	50.9	+2.4
TTL	43.28(1) ^{+0.38%} _{-1.09%}	36.6	42.83(1) ^{+0.17%} _{-0.72%}	36.8	+1.1
TLL	10.581(2) ^{+1.26%} _{-2.16%}	8.9	10.578(2) ^{+0.97%} _{-1.82%}	9.1	0.0
LLL	1.5998(4) ^{+1.41%} _{-2.27%}	1.4	1.5982(4) ^{+1.01%} _{-1.93%}	1.4	+0.1
Interference	2.176(7) ^{+1.66%} _{-2.16%}	1.8	2.182(7) ^{+1.39%} _{-1.63%}	1.9	-0.3

Table 1: Unpolarized and triply-polarized cross sections in attobarn (ab), together with the corresponding polarization fractions, calculated at LO using the TPA approach in the WWW c.m.f. for the process $pp \rightarrow W^- W^+ W^+ \rightarrow e^- \bar{\nu}_e \mu^+ \nu_\mu \tau^+ \nu_\tau + X$ using the central fixed and dynamical factorization scales. The corresponding full off-shell unpolarized cross sections are also provided. Statistical uncertainties are given in parentheses while scale uncertainties are provided in percentage as superscripts and subscripts. In the last column, the relative difference between the fixed and the dynamical scales is given for the cross sections.

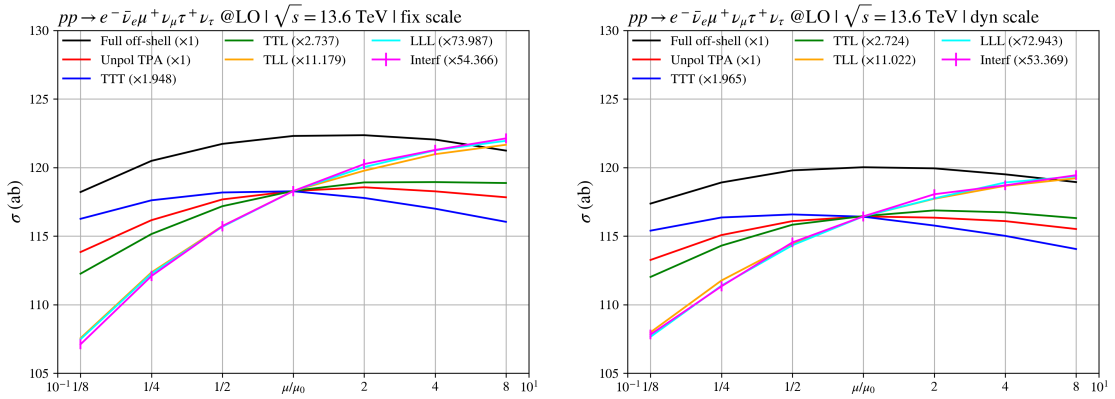


Figure 2: Cross sections as functions of the factorization scale parameter $\xi = \mu/\mu_0$ for fixed (left) and dynamical (right) scales. The vertical bars on the interference curve represent the statistical errors.

We first observe that, for the cross sections, the difference between the fixed scale and the dynamical scale is less than 3%, in magnitude, for all cases. The scale uncertainties reflect this difference in the TTL, TLL, LLL, and interference cases. For the remaining cases of unpolarized and TTT cross sections, the scale uncertainties are too small. This can be understood by looking at Fig. 2. The central scale $\mu = \mu_0$ is near the maximum position for the unpolarized and TTT cases, leading to very small scale uncertainties.

It is however not only the position of the central scale that is important but also the shape of the scale dependence. The slope increases with the addition of longitudinal mode. There are big changes going from TTT to TTL and to TLL, while the change is significantly reduced from TLL to LLL.

It is interesting to note the size of the interference fraction, about 2% for both scale choices. Using the other on-shell mappings gives the same result. For the process $W^+W^-W^-$, it is slightly smaller, of 1.6%, as shown in Appendix A. The scale uncertainties of the interference cross section are around 2% for both fixed and dynamical scales, being of the same size as those of the LLL and TLL polarizations. These values are larger than the difference between the fixed-scale and dynamical-scale cross sections. These scale uncertainties can be better understood by looking at the scale dependence in Fig. 2. We see that the μ dependence of the interference contribution is very similar to the LLL one. For the $W^+W^-W^-$ process, there is a clearer difference between them, as shown in Fig. 6, with the interference term increasing faster with the scale.

We now discuss the issue of scale choice. For integrated cross sections, it seems that both fixed and dynamical scales are good choices because the dominant contribution comes from the triple-resonance threshold region. This argument is also valid for diboson VV' productions. Here the fixed scale of $\mu_0 = (M_V + M_{V'})/2$ is commonly used because it gives larger cross sections which agree better with the measurement values. For differential cross sections, it has been widely recognized that dynamical scale is a better choice, in particular for transverse momentum or invariant mass distributions at high-energy regions.

The scale dependence shown in Fig. 2 gives us a new view on this issue. While for the unpolarized and TTT cross sections both choices gives the same dependence across the range of $\mu/\mu_0 \in [1/8, 8]$, the factorization scale dependence is significantly improved when using the dynamical scale for the TTL, TLL, LLL, and interference cross sections. We will therefore use the dynamical scale as the default choice for both integrated and differential cross sections.

Finally, we close this section by noting the smallness of the LLL fraction, being 1.4% and smaller than the interference term. With increasing number of longitudinal modes, the ratios $\sigma_{\text{TTL}}/\sigma_{\text{TTT}}$, $\sigma_{\text{TLL}}/\sigma_{\text{TTL}}$, and $\sigma_{\text{LLL}}/\sigma_{\text{TTL}}$ are 0.72, 0.25, and 0.15 for the dynamical scale, respectively. These values are essentially the same for the fixed scale case or for the $W^+W^-W^-$ process (see Appendix A for precise numbers). For comparison, the LO ratios $\sigma_{\text{TL}}/\sigma_{\text{TT}}$ and $\sigma_{\text{LL}}/\sigma_{\text{TL}}$ (TL here means TL+LT) are 0.31 and 0.30 for W^+W^- [23, 33], 0.29 and 0.38 for W^+Z [34], 0.32 and 0.38 for W^-Z [7], 0.34 and 0.25 for ZZ [24].

As radiative corrections are very similar between triboson and diboson processes, it is worth summarizing here the higher-order results available for the diboson case. We are interested in the change of the polarization fractions calculated in the VV c.m.f. when going from LO to (N)NLO QCD. For the W^+W^- process without jet veto and excluding the bottom-quark contribution, the f_{LL} changes from 6.6% [23] at LO to 5.7% at NLO QCD [35]. For the W^+Z process [8], it goes from 7.9% at LO to 5.7% at NLO QCD+EW, and to 5.6% at NNLO QCD + NLO EW. For the W^-Z process [7], it is 8.6% at LO and 5.9% at NLO QCD. For the ZZ case [24], it varies from 5.8% at LO to 5.9% at NLO QCD, and to 6.1% at NNLO QCD. The NLO EW corrections are negligible. NNLO QCD results

for the W^+W^- are provided in [16] but not usable here because they are calculated in the Lab frame. One thus sees that higher-order effects are mildest for the ZZ case where they increase the LL fractions slightly. For the remaining cases involving the W boson the effects are significantly stronger, but negative. The largest reduction is 31% when going from LO to NLO QCD for the W^-Z process, and the smallest reduction is 14% for the W^+W^- case. The same survey for the TL fraction gives positive corrections, ranging from +7% for ZZ , +20% for W^+W^- , +41% for W^-Z , +48% for W^+Z when going from LO to NLO QCD. NNLO QCD corrections are much smaller. From these results, we see that higher-order corrections affect different polarization fractions in different ways. It is therefore possible that the LLL fraction would get a positive correction from higher-order effects. However, this enhancement is not expected to exceed 100%. It is still very challenging to measure the σ_{LLL} at the LHC even in this optimistic scenario.

3.3 Kinematic distributions

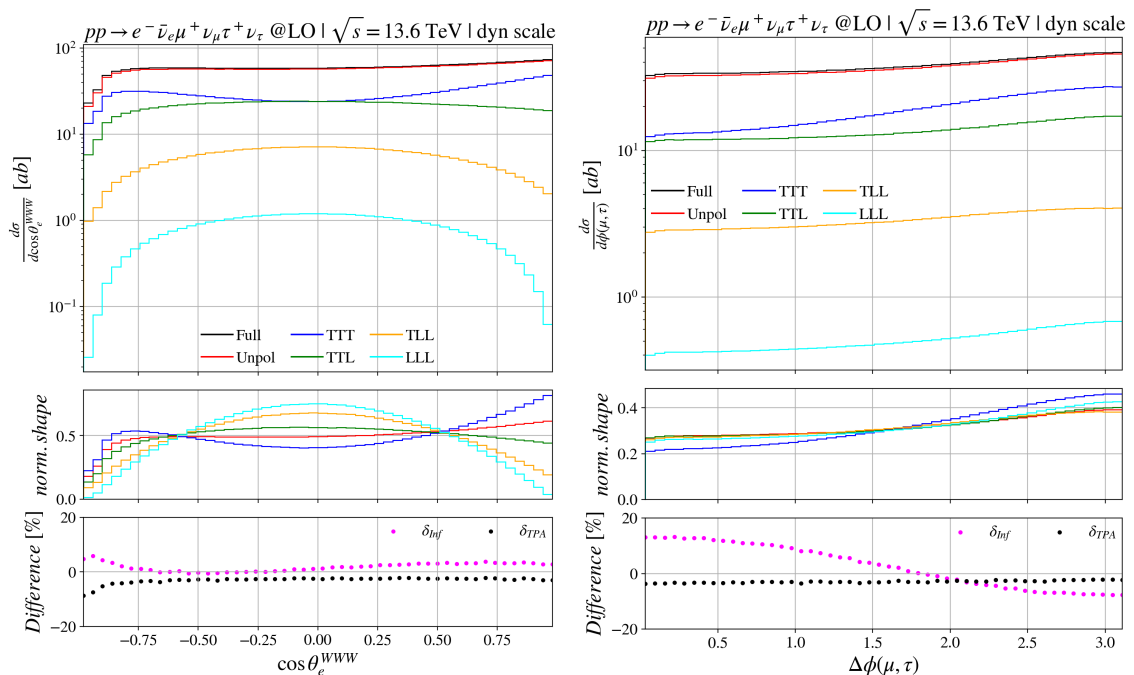


Figure 3: Distributions in $\cos\theta_e^{WWW}$ (left) and in azimuthal-angle difference between the muon and the tauon (right) are shown. The polar angle θ_e^{WWW} is defined in the WWW c.m.f. (see the text for details). The top panels show the values of the LO differential cross sections. The middle panels show the normalized distributions (areas are equal to unity), while the bottom panels display the interference contribution and the off-shell effect (difference between the unpolarized TPA and the full off-shell).

We now present results for some kinematic distributions, which are important for the measurement of polarized cross sections. They are displayed in Fig. 3, Fig. 4, Fig. 5 for the $W^-W^+W^+$ process. Corresponding results for the $W^+W^-W^-$ process are shown in Fig. 7,

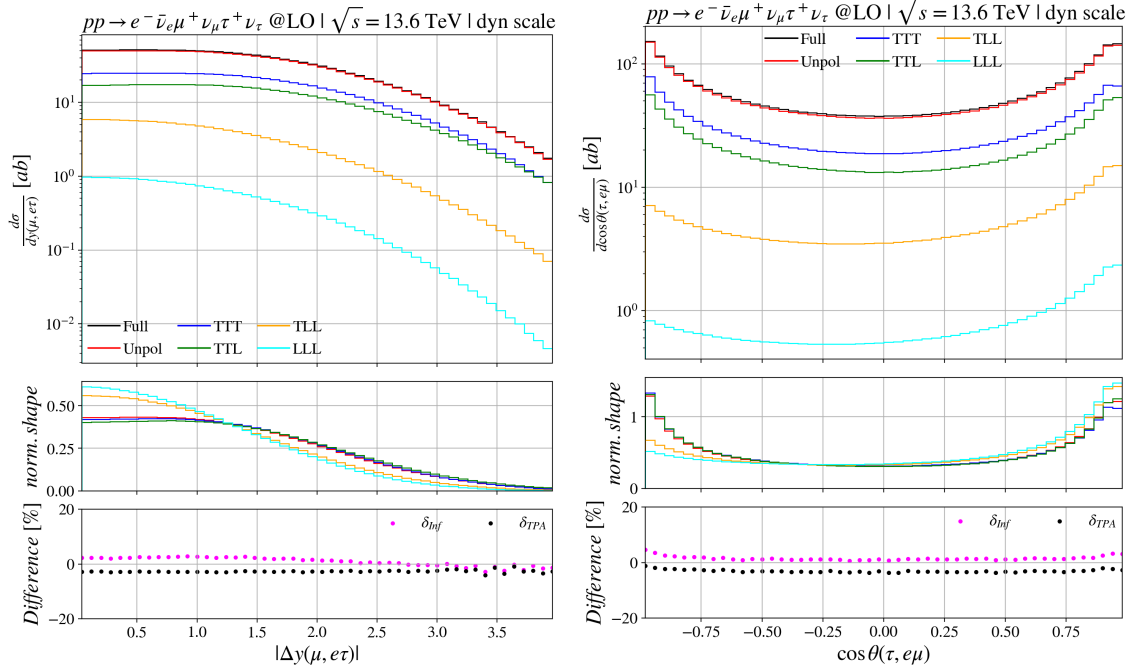


Figure 4: Same as Fig. 3 but for the rapidity difference between the muon and the electron-tauon system (left) and cosine of the angle between the tauon and the electron-muon system (right).

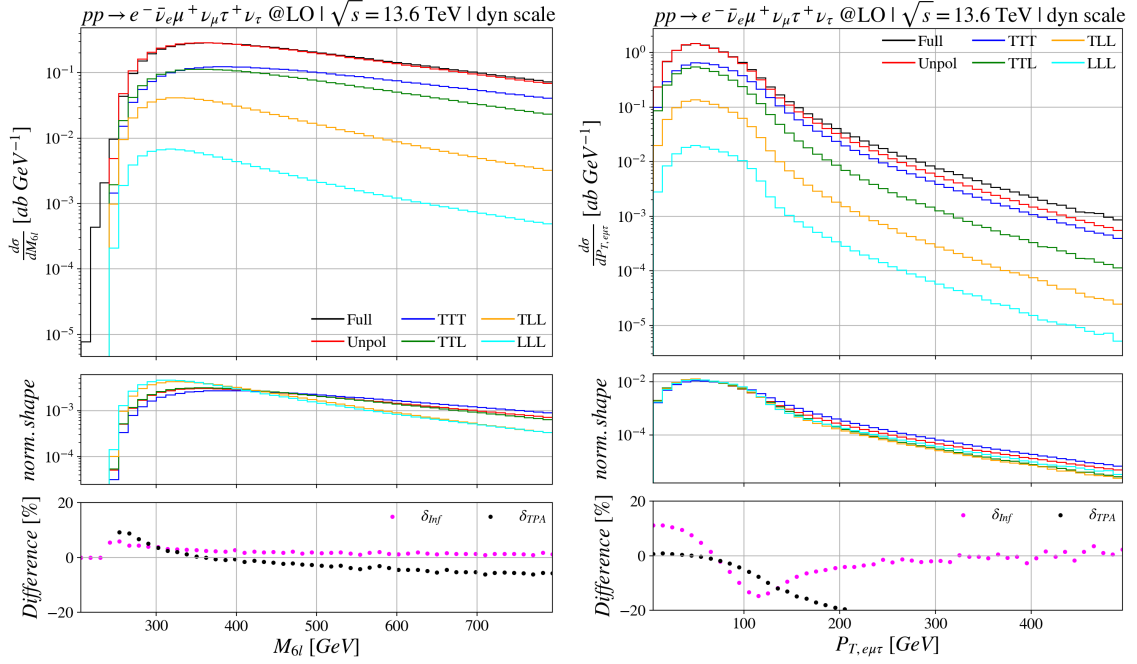


Figure 5: Same as Fig. 3 but for the invariant mass of the six-lepton system (left) and the transverse momentum of the electron-muon-tauon system (right).

Fig. 8, Fig. 9. All kinematic observables (x axis) are calculated in the Lab frame, except for the $\cos\theta_e^{WWW}$ in Fig. 3. This polar angle is calculated as the angle between $\vec{p}_{W^-}^{\text{rest}}$ (momentum direction of the electron measured in the parent W^- rest frame) and $\vec{p}_{WWW\text{-cmf}}^{W^-}$ (momentum of the W^- in the WWW c.m.f.). It is important to calculate $\vec{p}_{W^-}^{\text{rest}}$ from \vec{p}_{Lab}^e via two boosts: first boost from the Lab frame to the WWW c.m.f., second boost from the WWW c.m.f. to the W^- rest frame, as we are calculating the electron angle with respect to the W direction in the WWW c.m.f.. Boosting p_e directly from the Lab frame to the W^- rest frame would give a different direction.

For template fits of polarized cross sections, one has to rely on a distinguished shape of a given polarization. The $\cos\theta_e^{WWW}$ distribution in Fig. 3 (left) gives distinctly different shapes for the four polarizations, the $\Delta\phi(\mu, \tau)$ in Fig. 3 (right) can distinguish clearly the TTT. The $|\Delta y(\mu, e\tau)|$ and $\cos\theta(\tau, e\mu)$ distributions in Fig. 4 help to classify the four polarizations into two shapes, with one category for the TLL and LLL the other for the TTT and TTL. These kinds of angular distributions are therefore very helpful for the measurement of polarized cross sections.

The energy dependence of the polarized cross sections are plotted in Fig. 5. For the M_{6l} distribution (left), one would naively expect that, as the energy grows, the slope of the curve would increase with the number of longitudinal modes. This is clearly so for the cases of TTT, TTL, and TLL, with significant changes. However, the change from TLL to LLL is very mild. It is also interesting to notice the peak position of the differential cross sections. As the M_{6l} approaches the triple-resonance threshold of $3M_W \approx 241$ GeV, looking at the normalized-shape panel, one sees that the LLL rises fastest, followed by the TLL, TTL, and TTT. The peak position of the LLL is therefore a bit shifted to the left of the threshold, while it is shifted to the right of the threshold for the TTT. The interference between the four polarization modes is highest around the threshold, being about 5% (purple line in the bottom panel), and then drops as the energy increases.

Finally, the transverse momentum distribution of the $e - \mu - \tau$ system is plotted in Fig. 5 (right). At LO, this is identical to the missing transverse momentum distribution. As the transverse momentum grows, all polarized cross sections reach the peak at around 50 GeV and then go down slowly. Then, suddenly, something happens at around 120 GeV where the LLL cross section drops sharply. This also happens to the TLL and TTL, but with a lesser extent. Also at this position we begin seeing the different shape of the TTT compared to the other polarizations. The difference between the unpolarized TPA and the full off-shell differential cross sections is also becoming more and more visible from here. In addition, the polarization interference reaches a minimum at this position.

This remarkable different behavior of the LLL differential cross section is an indication of the usefulness of the LLL polarization. It can help to better understand the underlying dynamics of a phenomenon or, as one can imagine, to fit a model parameter (e.g. M_W) when there is a strong sensitivity. Before deciding on its application, one should however include radiative corrections to see whether this distinct behavior is smeared out.

The large differences between the unpolarized TPA and the full off-shell cross sections (see the black line in the bottom panel) at large $P_{T,e\mu\tau}$ have been observed in [17]. As pointed out there, this comes from two kinematic configurations. In one case, the large

$P_{T,\text{miss}}$ is balanced against a single charged-lepton $P_{T,\ell}$ with the P_T of the remaining charged leptons being soft. In the other case, the large $P_{T,e\mu\tau}$ recoils against a single neutrino transverse momentum while the other neutrinos are soft. These mechanisms are illustrated by the Feynman diagram in Fig. 1 (g, h), classified as a single-resonance contribution.

Concerning the comparison between the fixed and dynamical scales, integrated results in Table 1 show small differences. This is also the case for flat distributions such as angular distributions, where the deviations are within 5% across the whole range. For other distributions such as $P_{T,\ell}$, $M_{\ell\ell'}$, $\Delta y(\mu, e\tau)$, etc the differences can reach the level of tens of percent in the regions where the differential cross section is suppressed. These differences should be within the theory uncertainty bands.

4 Conclusions

We have presented, for the first time, all triply-polarized cross sections for the WWW production processes at the LHC. Results were obtained at LO with fully leptonic decays.

We found that the LLL cross section is very small at the integrated or differential cross section level. Higher order corrections are not expected to change this feature significantly. It is therefore very challenging to measure it.

It was also found that the polarization interference is of the same size as the LLL contribution. A separate template for the interference would then be needed in the measurement.

Compared to the diboson processes, a new ingredient for triboson processes is the on-shell mapping. We have presented a new and general method for all triboson processes. The essential idea is a dynamic and democratic mapping. Compared to the method proposed by Dittmaier and Schwan in [22] where the TPA conditions are hidden, our mapping shows clearly the TPA conditions. Numerically, the two methods give very similar results, though.

As a compensation for being small in cross section, triboson processes have numerous kinematic distributions with high power in shape distinction for different polarizations, in particular distributions in various angles between the flight directions of the charged leptons. Some representatives of those have been shown in this study. These distributions will be important for polarization measurements.

The next natural step is to calculate NLO corrections to see how the LLL fraction and the interference change. This is still work in progress.

A Results for the $W^+W^-W^-$ process

In this appendix results for the process $pp \rightarrow e^+\nu_e\mu^-\bar{\nu}_\mu\tau^-\bar{\nu}_\tau + X$ (named $W^+W^-W^-$ for short) are provided. Integrated cross sections are given in Table 2 and Fig. 6, while differential distributions are displayed in Fig. 7, Fig. 8, and Fig. 9.

	σ_{fix} [ab]	f_{fix} [%]	σ_{dyn} [ab]	f_{dyn} [%]	δ_σ [%]
Full off-shell	$67.293(8)^{+0.50\%}_{-1.06\%}$	–	$66.574(8)^{+0.20\%}_{-0.78\%}$	–	+1.1
Unpol. TPA	$65.51(1)^{+0.48\%}_{-1.17\%}$	100	$64.88(1)^{+0.19\%}_{-0.94\%}$	100	+1.0
TTT	$32.416(6)^{+0.00\%}_{-0.67\%}$	49.5	$31.887(6)^{+0.00\%}_{-0.35\%}$	49.1	+1.7
TTL	$24.384(5)^{+0.85\%}_{-1.53\%}$	37.2	$24.263(5)^{+0.47\%}_{-1.18\%}$	37.4	+0.5
TLL	$6.638(1)^{+1.63\%}_{-2.63\%}$	10.1	$6.657(1)^{+1.23\%}_{-2.07\%}$	10.3	–0.3
LLL	$1.0284(2)^{+1.77\%}_{-2.63\%}$	1.6	$1.0309(2)^{+1.42\%}_{-2.09\%}$	1.6	–0.2
Interference	$1.030(3)^{+2.30\%}_{-3.01\%}$	1.6	$1.045(4)^{+1.14\%}_{-2.93\%}$	1.6	–1.4

Table 2: Same as Table 1 but for the process $pp \rightarrow e^+\nu_e\mu^-\bar{\nu}_\mu\tau^-\bar{\nu}_\tau + X$.

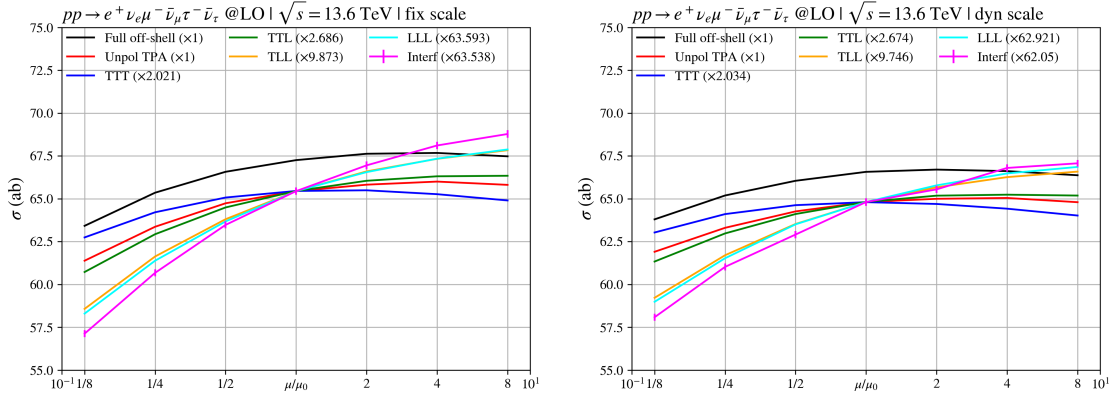


Figure 6: Same as Fig. 2 but for the process $pp \rightarrow e^+\nu_e\mu^-\bar{\nu}_\mu\tau^-\bar{\nu}_\tau + X$.

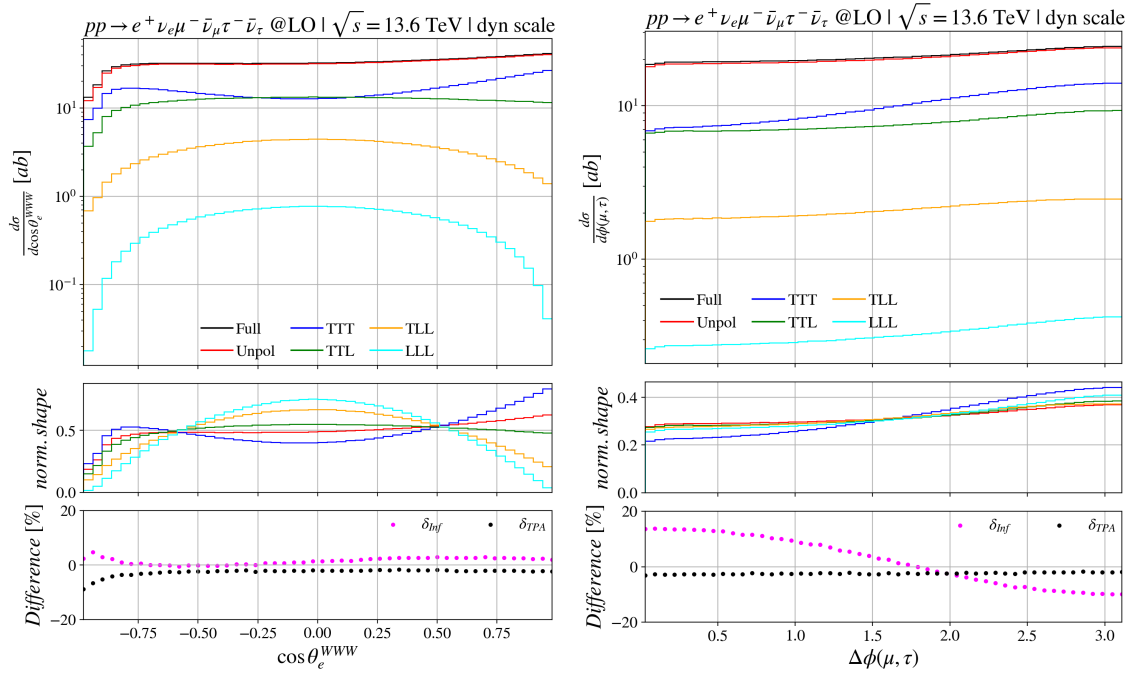


Figure 7: Same as Fig. 3 but for the process $pp \rightarrow e^+ \nu_e \mu^- \bar{\nu}_\mu \tau^- \bar{\nu}_\tau + X$.

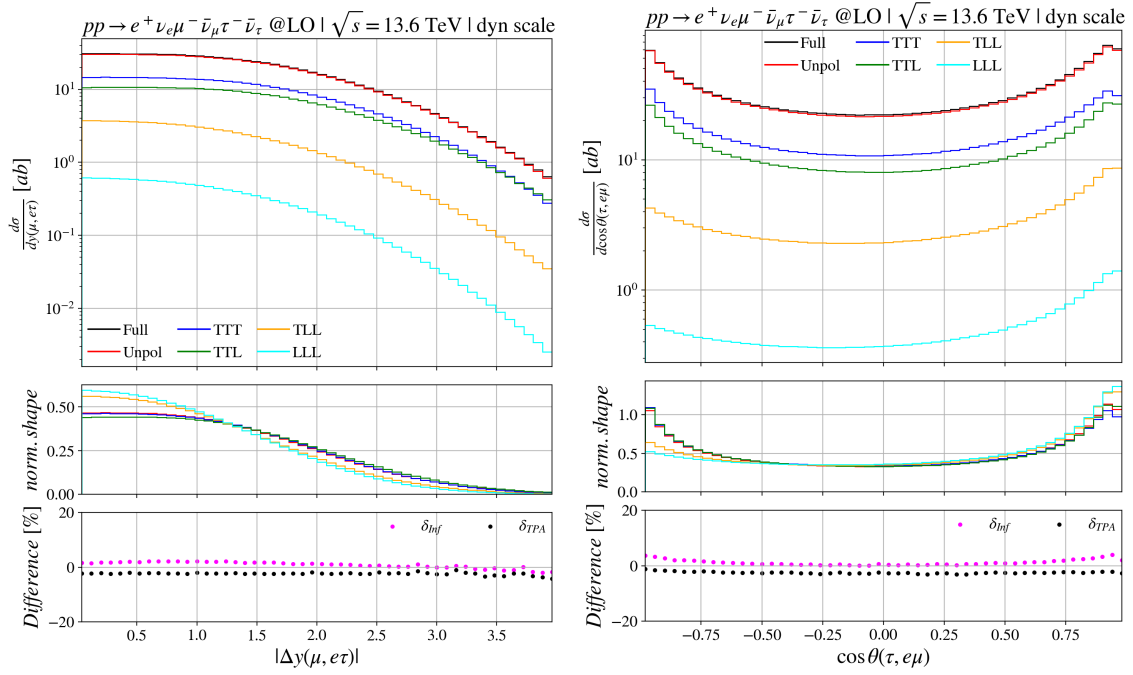


Figure 8: Same as Fig. 3 but for the rapidity difference between the muon and the electron-tau system (left) and cosine of the angle between the tauon and the electron-muon system (right) of the process $pp \rightarrow e^+ \nu_e \mu^- \bar{\nu}_\mu \tau^- \bar{\nu}_\tau + X$.

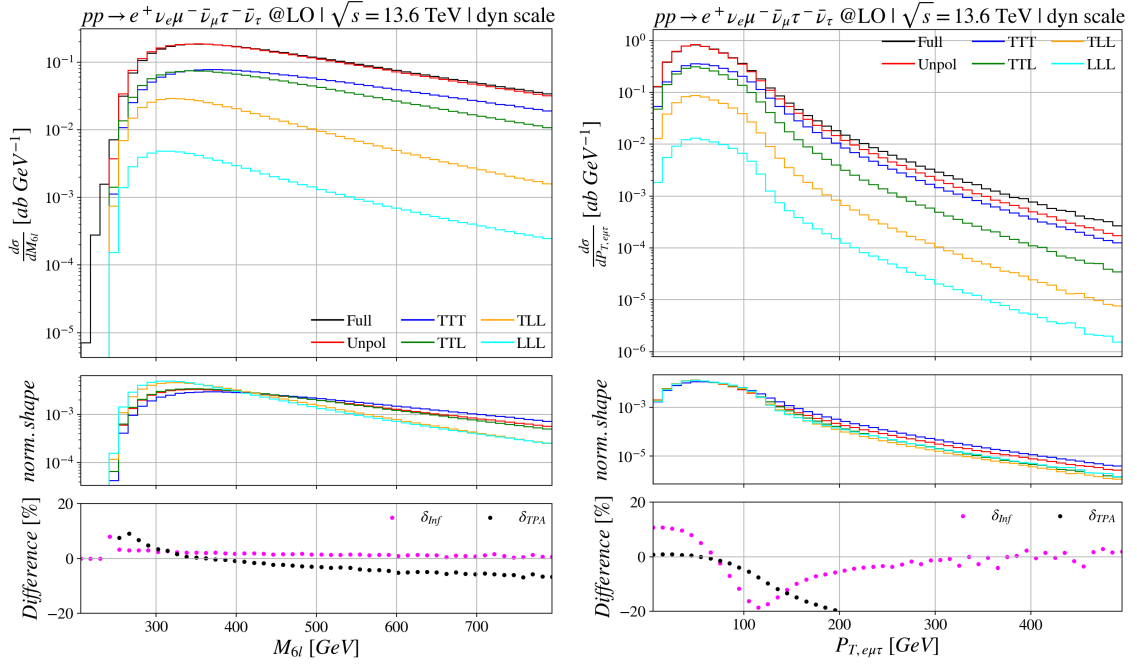


Figure 9: Same as Fig. 3 but for the invariant mass of the six-lepton system (left) and the transverse momentum of the electron-muon-tauon system (right) of the process $pp \rightarrow e^+ \nu_e \mu^- \bar{\nu}_\mu \tau^- \bar{\nu}_\tau + X$.

Acknowledgments

This research is funded by Phenikaa University under grant number PU2023-1-A-18.

References

- [1] CMS collaboration, *Measurement of the inclusive and differential WZ production cross sections, polarization angles, and triple gauge couplings in pp collisions at $\sqrt{s} = 13$ TeV*, *JHEP* **07** (2022) 032 [[2110.11231](#)].
- [2] ATLAS collaboration, *Studies of the Energy Dependence of Diboson Polarization Fractions and the Radiation-Amplitude-Zero Effect in WZ Production with the ATLAS Detector*, *Phys. Rev. Lett.* **133** (2024) 101802 [[2402.16365](#)].
- [3] ATLAS collaboration, *Evidence for Longitudinally Polarized W Bosons in the Electroweak Production of Same-Sign W Boson Pairs in Association with Two Jets in pp Collisions at $\sqrt{s} = 13$ TeV with the ATLAS Detector*, *Phys. Rev. Lett.* **135** (2025) 111802 [[2503.11317](#)].
- [4] ATLAS collaboration, *Observation of quantum entanglement with top quarks at the ATLAS detector*, *Nature* **633** (2024) 542 [[2311.07288](#)].
- [5] CMS collaboration, *Measurements of polarization and spin correlation and observation of entanglement in top quark pairs using lepton+jets events from proton-proton collisions at $s=13$ TeV*, *Phys. Rev. D* **110** (2024) 112016 [[2409.11067](#)].

- [6] A. Denner and G. Pelliccioli, *NLO EW and QCD corrections to polarized ZZ production in the four-charged-lepton channel at the LHC*, *JHEP* **10** (2021) 097 [[2107.06579](#)].
- [7] D.N. Le, J. Baglio and T.N. Dao, *Doubly-polarized WZ hadronic production at NLO QCD+EW: calculation method and further results*, *Eur. Phys. J. C* **82** (2022) 1103 [[2208.09232](#)].
- [8] G. Pelliccioli and R. Poncelet, *Precise predictions for joint polarisation fractions in WZ production at the LHC*, [2510.25898](#).
- [9] A. Denner, R. Franken, C. Haitz, D. Lombardi and G. Pelliccioli, *Electroweak corrections to doubly polarised WZ scattering at the LHC*, *JHEP* **02** (2026) 120 [[2510.26462](#)].
- [10] A. Denner, C. Haitz and G. Pelliccioli, *NLO EW and QCD corrections to polarised same-sign WW scattering at the LHC*, *JHEP* **11** (2024) 115 [[2409.03620](#)].
- [11] G. Pelliccioli and G. Zanderighi, *Polarised-boson pairs at the LHC with NLOPS accuracy*, *Eur. Phys. J. C* **84** (2024) 16 [[2311.05220](#)].
- [12] M. Hoppe, M. Schönherr and F. Siegert, *Polarised cross sections for vector boson production with Sherpa*, *JHEP* **04** (2024) 001 [[2310.14803](#)].
- [13] A. Denner, S. Dittmaier, M. Roth and D. Wackerth, *Electroweak radiative corrections to $e^+e^- \rightarrow WW \rightarrow 4$ fermions in double pole approximation: The RACOONWW approach*, *Nucl. Phys. B* **587** (2000) 67 [[hep-ph/0006307](#)].
- [14] A. Aeppli, F. Cuypers and G.J. van Oldenborgh, *$\mathcal{O}(\Gamma)$ corrections to W pair production in e^+e^- and $\gamma\gamma$ collisions*, *Phys. Lett. B* **314** (1993) 413 [[hep-ph/9303236](#)].
- [15] A. Aeppli, G.J. van Oldenborgh and D. Wyler, *Unstable particles in one loop calculations*, *Nucl. Phys. B* **428** (1994) 126 [[hep-ph/9312212](#)].
- [16] R. Poncelet and A. Popescu, *NNLO QCD study of polarised W^+W^- production at the LHC*, *JHEP* **07** (2021) 023 [[2102.13583](#)].
- [17] S. Dittmaier, G. Knippen and C. Schwan, *Next-to-leading-order QCD and electroweak corrections to triple-W production with leptonic decays at the LHC*, *JHEP* **02** (2020) 003 [[1912.04117](#)].
- [18] A. Denner, S. Dittmaier, M. Roth and D. Wackerth, *Predictions for all processes $e^+e^- \rightarrow 4$ fermions + gamma*, *Nucl. Phys. B* **560** (1999) 33 [[hep-ph/9904472](#)].
- [19] A. Denner, S. Dittmaier, M. Roth and L.H. Wieders, *Electroweak corrections to charged-current $e^+e^- \rightarrow 4$ fermion processes: Technical details and further results*, *Nucl. Phys. B* **724** (2005) 247 [[hep-ph/0505042](#)].
- [20] A. Denner and S. Dittmaier, *The Complex-mass scheme for perturbative calculations with unstable particles*, *Nucl. Phys. B Proc. Suppl.* **160** (2006) 22 [[hep-ph/0605312](#)].
- [21] J. Baglio and L.D. Ninh, *Fiducial polarization observables in hadronic WZ production: A next-to-leading order QCD+EW study*, *JHEP* **04** (2019) 065 [[1810.11034](#)].
- [22] S. Dittmaier and C. Schwan, *Non-factorizable photonic corrections to resonant production and decay of many unstable particles*, *Eur. Phys. J. C* **76** (2016) 144 [[1511.01698](#)].
- [23] T.N. Dao and D.N. Le, *NLO electroweak corrections to doubly-polarized W^+W^- production at the LHC*, *Eur. Phys. J. C* **84** (2024) 244 [[2311.17027](#)].
- [24] C. Carrivale et al., *Precise standard-model predictions for polarised Z-boson pair production and decay at the LHC*, *Eur. Phys. J. C* **85** (2025) 1342 [[2505.09686](#)].

- [25] T. Hahn, *Generating Feynman diagrams and amplitudes with FeynArts 3*, *Comput.Phys.Commun.* **140** (2001) 418.
- [26] T. Hahn and M. Perez-Victoria, *Automatized one-loop calculations in four and D dimensions*, *Comput. Phys. Commun.* **118** (1999) 153.
- [27] G.P. Lepage, *A New Algorithm for Adaptive Multidimensional Integration*, *J. Comput. Phys.* **27** (1978) 192.
- [28] S. Kawabata, *A New version of the multidimensional integration and event generation package BASES/SPRING*, *Comput. Phys. Commun.* **88** (1995) 309.
- [29] J. Baglio et al., *Release note: VBFNLO 3.0*, *Eur. Phys. J. C* **84** (2024) 1003 [2405.06990].
- [30] NNPDF collaboration, *The path to proton structure at 1% accuracy*, *Eur. Phys. J. C* **82** (2022) 428 [2109.02653].
- [31] A. Buckley, J. Ferrando, S. Lloyd, K. Nordström, B. Page, M. Rüfenacht et al., *LHAPDF6: parton density access in the LHC precision era*, *Eur. Phys. J. C* **75** (2015) 132 [1412.7420].
- [32] PARTICLE DATA GROUP collaboration, *Review of particle physics*, *Phys. Rev. D* **110** (2024) 030001.
- [33] A. Denner, C. Haitz and G. Pelliccioli, *NLO EW corrections to polarised W^+W^- production and decay at the LHC*, *Phys. Lett. B* **850** (2024) 138539 [2311.16031].
- [34] D.N. Le and J. Baglio, *Doubly-polarized WZ hadronic cross sections at NLO QCD + EW accuracy*, *Eur. Phys. J. C* **82** (2022) 917 [2203.01470].
- [35] T.N. Dao and D.N. Le, *Polarized W^+W^- pairs at the LHC: Effects from bottom-quark induced processes at NLO QCD + EW*, *Eur. Phys. J. C* **85** (2025) 108 [2409.06396].